

Kullback-Leibler Divergence-Based Fuzzy C-Means Clustering Incorporating Morphological Reconstruction and Wavelet Frames for Image Segmentation

Cong Wang, Witold Pedrycz, *Fellow, IEEE*, ZhiWu Li, *Fellow, IEEE*, and MengChu Zhou, *Fellow, IEEE*

Abstract—Although spatial information of images can usually enhance the robustness of the conventional Fuzzy C-Means (FCM) algorithm, it greatly increases the computational costs for image segmentation. To achieve a sound trade-off between the segmentation performance and the speed of clustering, we come up with a Kullback-Leibler divergence-based FCM algorithm by incorporating a tight wavelet frame transform and a morphological reconstruction operation. To enhance FCM's robustness, an observed image is first filtered by using the morphological reconstruction. A tight wavelet frame system is employed to decompose the observed and filtered images so as to form their feature sets. Considering these feature sets as data of clustering, an modified FCM algorithm is proposed, which introduces a Kullback-Leibler divergence term in the partition matrix into its objective function. The Kullback-Leibler divergence term aims to make membership degrees of each image pixel closer to those of its neighbors, which brings that the membership partition becomes more suitable and the parameter setting of FCM becomes simplified. On the basis of the obtained partition matrix and prototypes, the segmented feature set is reconstructed by minimizing the inverse process of the modified objective function. To modify abnormal features produced in the reconstruction process, each reconstructed feature is reassigned to the closest prototype. As a result, the segmentation accuracy of Kullback-Leibler divergence-based FCM is further improved. What's more, the segmented image is reconstructed by using a tight wavelet frame reconstruction operation. Finally, supporting experiments coping with synthetic, medical and color images are reported. Experimental results exhibit that the proposed algorithm works well and comes with better segmentation performance than other comparative algorithms. Moreover, the proposed algorithm

requires less time than most of the FCM-related algorithms.

Index Terms—Fuzzy C-Means; image segmentation; Kullback-Leibler divergence; wavelet frame; morphological reconstruction.

I. INTRODUCTION

DUE to its simplicity, a Fuzzy C-Means (FCM) algorithm [1], [2] has been applied to a wide range of applications, such as image analysis [3], granular computing [4] and pattern recognition [5]. However, the conventional FCM algorithm only performs well for noisy-free image data [3]. To overcome its drawback, a collection of improved versions of FCM have been proposed by mainly considering spatial information [6]–[10] and kernel distances (functions) [11]–[15]. As to the first improvement, many FCM-related algorithms introduce a neighborhood term on spatial information into the objective function of FCM. For instance, Ahmed et al. [6] report an improved algorithm, namely FCM_S, by introducing a neighbor term into the FCM algorithm. Since FCM_S calculates the neighbor term in each iteration, its computational complexity is high. To improve the robustness of FCM_S, Chen and Zhang [7] introduce two variants of FCM_S, namely FCM_S1 and FCM_S2, by employing mean and median filters. However, the two algorithms require higher running time than FCM_S. To enhance their computational efficiency, Cai et al. [8] propose a fast generalized FCM algorithm (FGFCM) by using gray level histograms. Moreover, FGFCM also improves the segmentation performance of FCM by incorporating a local similarity measure. However, its drawback is to require more parameters to achieve a good trade-off between robustness to noise and effect of retaining feature details. Krinidis et al. [9] utilize a fuzzy factor to simplify the parameter settings in FGFCM, thus forming a fuzzy local information C-means algorithm (FLICM). Superior to FGFCM, FLICM has better segmentation performance and is free of parameters. Nevertheless, FLICM only adopts the non-robust Euclidean distance, thus it is not effective for arbitrary spatial information.

To further enhance the FLICM's robustness, the second improvement is investigated by augmenting kernel distances into the objective function of FLICM. The implication of kernel distances (functions) is to achieve the transformation from the original data space to a new data space. Due to superior properties of the new space, image data can be easily

This work was supported in part by the Doctoral Students' Short Term Study Abroad Scholarship Fund of Xidian University, in part by the National Natural Science Foundation of China under Grant Nos. 61873342, 61672400, in part by the Recruitment Program of Global Experts, and in part by the Science and Technology Development Fund, MSAR, under Grant No. 0012/2019/A1. (*Corresponding author: ZhiWu Li and MengChu Zhou.*)

C. Wang is with the School of Electro-Mechanical Engineering, Xidian University, Xi'an 710071, China (e-mail: wangc0705@stu.xidian.edu.cn).

W. Pedrycz is with the Department of Electrical and Computer Engineering, University of Alberta, Edmonton, AB T6R 2V4, Canada, the School of Electro-Mechanical Engineering, Xidian University, Xi'an 710071, China, and also with the Faculty of Engineering, King Abdulaziz University, Jeddah 21589, Saudi Arabia (e-mail: wpedrycz@ualberta.ca).

Z. Li is with the School of Electro-Mechanical Engineering, Xidian University, Xi'an 710071, China, and also with the Institute of Systems Engineering, Macau University of Science and Technology, Macau, China (e-mail: zhwli@xidian.edu.cn).

M. Zhou is with the Institute of Systems Engineering, Macau University of Science and Technology, Macau 999078, China and also with the Helen and John C. Hartmann Department of Electrical and Computer Engineering, New Jersey Institute of Technology, Newark, NJ 07102 USA (e-mail: zhou@njit.edu).

manipulated and analyzed, thus resulting in a collection of kernel-based FCM algorithms [11]–[15]. For example, Gong et al. [11] introduce a tradeoff weighted fuzzy factor and a kernel metric to improve the robustness of FLICM, which forms a novel algorithm, namely KWFLICM. This algorithm works well for different types of noise, but it is extremely time-consuming. Zhao et al. [12] propose a neighborhood weighted FCM clustering algorithm (NWFCM) by replacing a Euclidean distance with a neighborhood weighted distance. Compared with FLICM and KWFLICM, NWFCM exhibits higher computational efficiency. However, the usage of the patch distance and setting of several parameters make NWFCM's computational efficiency lower than computing overhead of many FCM-related algorithms. Moreover, Wang et al. [13] present a wavelet frame-based FCM algorithm (WFCM) for segmenting images defined in non-flat domains. The main superiority of WFCM is to employ tight wavelet frames to form feature spaces of images. On the basis of these feature spaces, the image data characteristics can be analyzed well. Therefore, WFCM achieves good segmentation performance.

In addition, for the sake of the improvement of robustness and computational efficiency of FCM, some comprehensive FCM-related algorithms has been recently reported [16]–[19], which involve varying mathematical techniques, like Kullback-Leibler (KL) divergence [16], morphological gray reconstruction [18] and sparse representation [19]. Typically, Gharieb et al. [16] introduce the KL divergence to restrain local memberships, which achieves the improvement for the conventional FCM algorithm. Whereas, the derived algorithm exhibits low computational efficiency and its performance can be further improved. Lei et al. [18] come up with a fast and robust FCM algorithm (FRFCM) based on morphological gray reconstruction and membership filtering. FRFCM is so fast due to the use of gray level histograms. However, its performance is sometimes unstable. More recently, Zhang et al. [19] propose two alternative clustering algorithms, namely DSFCM and DSFCM_N, which introduce sparse regularization in terms of deviations into the objective function of FCM. Once spatial information is encountered, DSFCM upgrades to DSFCM_N that makes full use of neighbor information. Although the two algorithms provide a new avenue for image segmentation, their performance can further be improved.

By reviewing the literature, we conclude that existing algorithms cannot consider well the trade-off between the segmentation performance and the speed of clustering. Although most of algorithms improve the FCM's robustness to some extent, their computing overheads are usually large due to multiple factors, such as the use of image patch, parameter selection, and high-dimensional data space. Even though a small proportion of algorithms make some efforts to reduce the computational costs, like using gray level histograms and improving non-Euclidean distances, their segmentation effects can still be improved. In addition, we find that there is no work involves a deep discussion on the optimization of membership partition in order to improve FCM's performance. Although the work in [16] has roughly touched on optimizing local memberships by using the KL divergence, further discussion on the segmentation performance is not conducted and the

computational efficiency is low. In fact, membership grades of a specific image pixel are close to those of its neighborhoods. Hence, the optimization of the membership partition in each iteration can have a positive impact on the segmentation performance of FCM. To sum up, the improved FCM-related algorithms are still not well exploited, which exhibit good segmentation effects and require less time simultaneously.

To deal with this issue, inspired by [16], [18], we present a KL divergence-based FCM algorithm by incorporating a tight wavelet frame transform [20], [21] and a morphological reconstruction (MR) operation [22], [23], which realizes the optimization of membership partition and fast speed of clustering. Aiming to enhance FCM's robustness, an observed image is first filtered by using the MR. A tight wavelet frame system is employed to decompose the observed and filtered images so as to form their feature sets. Taking these feature sets as data of clustering, an modified FCM algorithm is proposed, which incorporates a KL divergence term in the partition matrix into its objective function. On the basis of the obtained partition matrix and prototypes, the segmented feature set is reconstructed by minimizing the inverse process of the modified objective function. To modify abnormal features produced in the reconstruction process, each reconstructed feature is reassigned to the closest prototype. In the sequel, the segmentation accuracy of KL divergence-based FCM is further improved. Finally, the segmented image is reconstructed by using a tight wavelet frame reconstruction operation. The framework of the proposed algorithm is drawn in Fig. 1.

As a whole, this study makes three contributions to the development of FCM. The first contribution is to employ the MR to filter the observed image, which means that spatial information of the image is introduced into clustering and the iterative calculation of a conventional local neighbor term is avoided. Therefore, the computational efficiency of FCM is enormously improved. In addition, the MR also overcomes the drawback of having to select different filters suitable for different types of noise, which is revealed in many improved FCM-related algorithms. In the sequel, the usage of the MR makes FCM more robust to different types of noise. Finally, the MR makes the distribution characteristic of image pixels favorable to fuzzy clustering, which is also positive to improve the speed of clustering.

The second contribution is to utilize tight wavelet frames to form feature sets of images, which thereby eliminates the defect of using image pixels. Since tight wavelet frames can acquire sparse approximations of an image, the underlying features in the image can be analyzed as much as possible. As a matter of fact, tight wavelet frames can be viewed as a kernel function, thus forming a kernel-based FCM algorithm. The essence of the kernel function is to achieve the transformation from the original space (time domain) to a new feature space (frequency domain). Thus, the underlying features and noise in images can be easily found.

Finally, we introduce a KL divergence term to the membership partition is introduced into the objective function of FCM. With the assistance of the KL divergence term, membership grades of a specific image pixel are close to those of its neighborhoods. Therefore, the optimization of membership partition

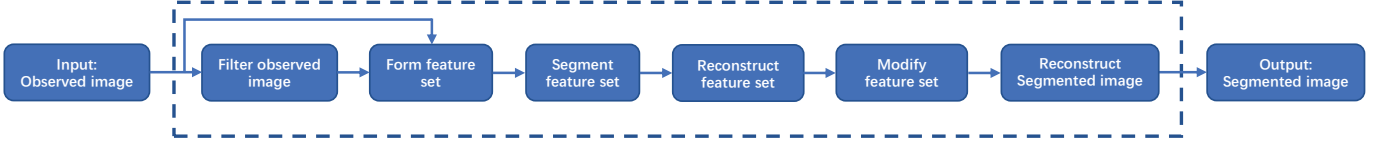


Fig. 1. The framework of the proposed algorithm.

in each iteration have a positive impact on the segmentation performance of FCM. In addition, for further improvement of the segmentation accuracy of KL divergence-based FCM, we minimize the inverse process of the modified objective function to reconstruct the segmented feature set. To modify abnormal features produced in the reconstruction process, each reconstructed feature is reassigned to the closest prototype. Finally, it is worth mentioning that the usage of KL divergence makes the fuzzification coefficient not present in FCM. Hence, the parameter setting of FCM becomes simplified.

In conclusion, this work presents a distinct originality that the proposed algorithm is a fast and robust FCM method by using some potential measures. The FCM algorithm is conducted in the feature spaces produced by tight wavelet frames, which is useful to manipulate image features and noise. Even though the KL divergence has a positive impact on a partition matrix, it also results in a high computing overhead. Whereas, the use of the MR makes up for the drawback caused by KL divergence since it acts as a pre-processing step to introduce spatial information into FCM in advance, implying that the iterative calculation of a conventional local neighbor term is avoided. The noise-immunity and retention capacity of image details are meanwhile exhibited. In addition, in order to further enhance the segmentation effects, the reconstruction of the segmented feature set is designed. Finally, the parameter setting of FCM is simplified since the usage of KL divergence makes the fuzzification coefficient not present in the proposed algorithm.

The structure of this paper is arranged as follows. Section II briefly describes the FCM algorithm and a tight wavelet frame transform. Section III formulates the proposed algorithm in detail. Section IV reports experimental results for synthetic, medical, and color images. Conclusions are reached in Section V.

II. PRELIMINARIES

A. FCM

Denote an image with K pixels as f . Since each image pixel often implies a set of attributes (variables), f can be formulated as $\mathbf{X} = \{\mathbf{x}_1, \mathbf{x}_2, \dots, \mathbf{x}_K\} \subset \mathbb{R}^K$. The FCM algorithm divides \mathbf{X} into several clusters by minimizing the objective function

$$J(\mathbf{U}, \mathbf{V}) = \sum_{i=1}^c \sum_{j=1}^K u_{ij}^m \|\mathbf{x}_j - \mathbf{v}_i\|^2, \quad (1)$$

subject to

$$\sum_{i=1}^c u_{ij} = 1, \text{ for } j \in \{1, 2, \dots, K\},$$

where $\mathbf{U} = [u_{ij}]_{c \times K}$ with $0 \leq u_{ij} \leq 1$ is a partition (membership) matrix, $\mathbf{V} = \{\mathbf{v}_i\}_{i=1,2,\dots,c}$ is a set of c prototypes, $\|\cdot\|$ denotes the Euclidean distance, and m is a fuzzification coefficient ($m > 1$).

The minimization of (1) can be realized by iteratively updating the partition matrix and the prototypes [24]:

$$u_{ij} = \frac{(\|\mathbf{x}_j - \mathbf{v}_i\|^2)^{-\frac{1}{m-1}}}{\sum_{q=1}^c (\|\mathbf{x}_j - \mathbf{v}_q\|^2)^{-\frac{1}{m-1}}} \text{ and } \mathbf{v}_i = \frac{\sum_{j=1}^K u_{ij}^m \mathbf{x}_j}{\sum_{j=1}^K u_{ij}^m}.$$

By presetting a nonnegative threshold ε , the algorithm iterates until $\|\mathbf{U}^{(t)} - \mathbf{U}^{(t-1)}\| < \varepsilon$ has been met. Here, t is an iteration index of the FCM algorithm.

B. Tight Wavelet Frame Transform

Wavelet frames exhibit powerful ability for feature/texture extraction. Thus they are applied to a wide range of research fields, such as image segmentation [13], image denoising [25]–[27], image restoration [20], and mesh surface reconstruction [28], [29]. For the sake of simplicity, we introduce the main idea of a tight wavelet frame transform. The reader is referred to [20], [21]. The tight wavelet frame transform involves two operators, i.e., decomposition \mathcal{W} and reconstruction \mathcal{W}^T . By collecting a set of filters (masks), \mathcal{W} can be generated based on γ sub-filtering operators, i.e., $\mathcal{W}_0, \mathcal{W}_1, \dots, \mathcal{W}_{\gamma-1}$. Among them, \mathcal{W}_0 is the low-pass filtering operator and the rest are high-pass filtering operators. With the assistance of unitary extension principle [30], \mathcal{W}^T can be available. Moreover, we have $\mathcal{W}^T \mathcal{W} f = f$, where $\mathcal{W}^T \mathcal{W}$ is an identity operation.

III. METHODOLOGY

A. Image Filtering via MR

As a pre-processing step, the MR is applied to filter an observed image, which improves FCM's robustness and makes the distribution characteristic of image pixels favorable to fuzzy clustering. Formally speaking, the MR is composed of two operators, i.e., dilation and erosion reconstructions [31]. Given two images f (mask image) and g (marker image), the dilation reconstruction is defined as

$$\mathcal{R}_f^{\mathcal{D}}(g) = \mathcal{D}_f^{(t)}(g),$$

where $\mathcal{D}_f^{(t)}(g)$ is formulated as

$$\mathcal{D}_f^{(t)}(g) = \begin{cases} \mathcal{D}(g) \wedge f, & t = 1 \\ \mathcal{D}(\mathcal{D}^{(t-1)}(g)) \wedge f, & t = 2, 3, \dots \end{cases}$$

where $g \leq f$, \wedge stands for the point-wise minimum and \mathcal{D} represents the dilation of g by a flat structuring element [23].

The erosion reconstruction is defined as

$$\mathcal{R}_f^\mathcal{E}(g) = \mathcal{E}_f^{(t)}(g),$$

where $\mathcal{E}_f^{(t)}(g)$ is formulated as

$$\mathcal{E}_f^{(t)}(g) = \begin{cases} \mathcal{E}(g) \vee f, & t = 1 \\ \mathcal{E}(\mathcal{E}^{(t-1)}(g)) \vee f, & t = 2, 3, \dots \end{cases}$$

where $g \geq f$, \vee stands for the point-wise maximum and \mathcal{E} represents the erosion of g by a flat structuring element.

Here, we select $g = \mathcal{E}(f)$ and $g = \mathcal{D}(f)$ as marker images for dilation and erosion reconstructions, respectively. According to the two reconstruction operators, the morphological closing reconstruction of f is given as

$$\mathcal{R}^C(f) = \mathcal{R}_{\mathcal{R}_f^\mathcal{E}(\mathcal{E}(f))}^\mathcal{D}(\mathcal{D}(\mathcal{R}_f^\mathcal{D}(\mathcal{E}(f)))). \quad (2)$$

In this work, f is an observed image and its filtered image is denoted as $\bar{f} = \mathcal{R}^C(f)$.

To illustrate the performance of the MR for feature preservation and noise suppression, we give an example, refer to Fig. 2. A square of size 3×3 is the structuring element.

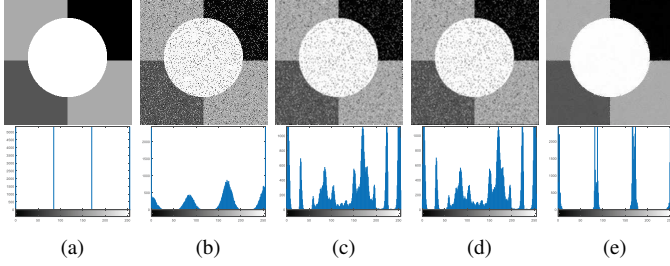


Fig. 2. Comparison with different filtering methods. (a) Original image. (b) Observed image. (c) Filtered result using a mean filter. (d) Filtered result using a median filter. (e) Filtered result using the MR.

The first row of Fig. 2 shows an original image, an observed image, and three filtered images that generated by a mean filter, a median filter, and the MR, respectively. The second row of Fig. 2 represents the corresponding gray level histograms. The original image includes four gray levels, i.e., 0, 85, 170, and 255. Obviously, its gray level histogram has four obvious peaks. We generate the observed image by imposing mixed Gaussian and impulse noise with $s = 10$ and $r = 10\%$ (additive white Gaussian noise with standard deviation s and salt and pepper impulse noise with density r) on the original image. The gray level histogram of the observed image only has two apparent peaks (0 and 255). As shown in Fig. 2(c)–(d), both mean and median filters produce too many peaks while the MR mainly splits the observed image into 4 clusters. Thus, the MR can effectively retain image details and remove noise simultaneously.

B. Feature Extraction via Wavelet Frames

On the basis of the observed image and filtered image generated by the MR, we can employ a tight frame system to form feature sets of the two images. In many applications, the piecewise linear B-spline tight frame system [30], [32] is

validated to be more adaptable to features and noise since it can provide redundant representations of images. Thus, we choose this system in which the corresponding filters are discretized as

$$a_0 = \left[\frac{1}{4}, \frac{1}{2}, \frac{1}{4} \right], a_1 = \left[-\frac{1}{4}, \frac{1}{2}, -\frac{1}{4} \right], a_2 = \left[\frac{\sqrt{2}}{4}, 0, -\frac{\sqrt{2}}{4} \right].$$

Using the above three one-dimensional filters, we can generate nine two-dimensional filters, including one low-pass filter and eight high-pass filters, which correspond to nine sub-filtering operators $\mathcal{W}_0, \mathcal{W}_1, \dots, \mathcal{W}_8$. They make up a tight wavelet frame decomposition operator \mathcal{W} . Hence, we can utilize the decomposition operator to form feature sets associated with the observed and filtered images, i.e.,

$$\mathbf{X} = \mathcal{W}f \text{ and } \bar{\mathbf{X}} = \mathcal{W}\bar{f}. \quad (3)$$

For image processing, \mathcal{W}_0f and $\mathcal{W}_0\bar{f}$ represent low frequency information, the rest represent high frequency information. The above formulation abstracts the feature extraction results obtained by the use of 1-level tight wavelet frame decomposition. The value of the decomposition level represents the number of times where the target data are sequentially decomposed. To better exhibit the effect of wavelet frames, we show an example, refer to Fig. 3.

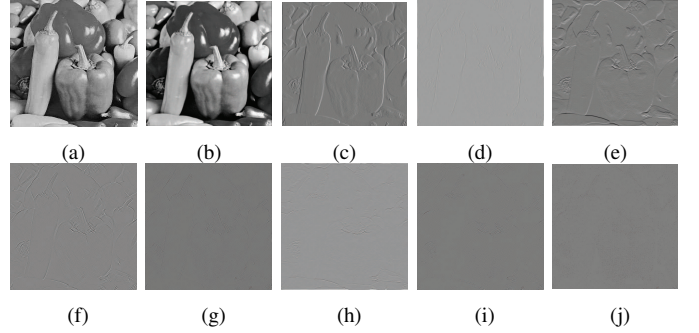


Fig. 3. Original image f and its wavelet coefficients. (a) Original image f ; (b)–(j) $\mathcal{W}_0f, \mathcal{W}_1f, \dots, \mathcal{W}_8f$.

As shown in Fig. 3, we find that 1-level tight wavelet frame decomposition gives redundant representations of a sampled image, thus forming a feature set of the image. The dimensionality of the feature set is nine times higher than the dimensionality of the sampled image. That is to say, each image pixel contains nine underlying attributes, i.e., one low frequency and eight high frequencies. Formally speaking, for an image with K pixels, the size of its feature set \mathbf{X} is $9 \times K$. Therefore, for image segmentation, the dimensionality of data of clustering is expanded when comparing with the direct use of image pixels.

C. KL Divergence-Based FCM

By introducing spatial information and tight wavelet frames, FCM becomes more robust to noise. To further improve its segmentation performance, we employ the KL divergence to optimize the partition matrix produced by FCM. We reformulate feature sets associated with f and \bar{f} as $\mathbf{X} = \mathcal{W}f =$

$\{\mathbf{x}_1, \mathbf{x}_2, \dots, \mathbf{x}_K\}$ and $\bar{\mathbf{X}} = \mathcal{W}\bar{\mathbf{f}} = \{\bar{\mathbf{x}}_1, \bar{\mathbf{x}}_2, \dots, \bar{\mathbf{x}}_K\}$. The modified objective function is expressed as

$$J(\mathbf{U}, \mathbf{V}) = \sum_{i=1}^c \sum_{j=1}^K u_{ij} (\|\mathbf{x}_j - \mathbf{v}_i\|^2 + \alpha \|\bar{\mathbf{x}}_j - \mathbf{v}_i\|^2) + \beta \sum_{i=1}^c \sum_{j=1}^K u_{ij} \log \frac{u_{ij}}{\bar{u}_{ij}}, \quad (4)$$

where α and β are positive parameters that control the impacts of the filtered term $\|\bar{\mathbf{x}}_j - \mathbf{v}_i\|^2$ and KL divergence term $\sum_{i=1}^c \sum_{j=1}^K u_{ij} \log \frac{u_{ij}}{\bar{u}_{ij}}$ on FCM, respectively. Note that the fuzzification coefficient is not present in this formulation of the objective function by introducing the KL divergence term that involves the original partition matrix $\mathbf{U} = [u_{ij}]_{c \times K}$ and the filtered partition matrix $\bar{\mathbf{U}} = [\bar{u}_{ij}]_{c \times K}$ that is defined as

$$\bar{\mathbf{U}} = \text{median}(\mathbf{U}). \quad (5)$$

Here, the operator *median* represents median filtering applied to each row of \mathbf{U} with a local window of a selected size, which means that abnormal membership grades in \mathbf{U} produced in each iteration are modified by their neighbors.

In particular, in [16], the KL divergence was first introduced into the objective function of FCM. However, different from our work, a mean filter is employed for constructing the KL divergence term. The mean filtering results are experimentally worse than those obtained by using a median filter. What is more, the work in [16] does not try to overcome the shortcomings that the usage of the KL divergence results in high computational complexity and spatial information of images are absent in the objective function of FCM.

We apply the Lagrange multiplier method to minimize (4). The iterative updates of the partition matrix \mathbf{U} and prototypes \mathbf{v}_i are given as follows:

$$u_{ij} = \frac{\bar{u}_{ij} e^{-(\|\mathbf{x}_j - \mathbf{v}_i\|^2 + \alpha \|\bar{\mathbf{x}}_j - \mathbf{v}_i\|^2)/\beta}}{\sum_{q=1}^c \bar{u}_{iq} e^{-(\|\mathbf{x}_j - \mathbf{v}_q\|^2 + \alpha \|\bar{\mathbf{x}}_j - \mathbf{v}_q\|^2)/\beta}}, \quad (6)$$

$$\mathbf{v}_i = \frac{\sum_{j=1}^K u_{ij} (\mathbf{x}_j + \alpha \bar{\mathbf{x}}_j)}{(1 + \alpha) \sum_{j=1}^K u_{ij}}. \quad (7)$$

The derivations are provided in the Appendix.

We cover an example to illustrate the impact of the KL divergence on FCM. We impose mixed Gaussian and impulse noise on an original image shown in Fig. 2(a). The noise level is set to $s = 30$ and $r = 20\%$. To better exhibit the impact of the KL divergence, we fix $\alpha = 1.5$ while the 1-level tight wavelet frame decomposition is present. The number of clusters is set to 4 because the original image contains four gray levels. As shown in Fig. 4, by introducing the KL divergence and setting $\beta = 15000$ (how to select the value of β will be discussed in Section IV-A), an arbitrary image pixel has close membership degrees to those of its neighbors, which means that the membership partition becomes more suitable and classification errors are reduced.

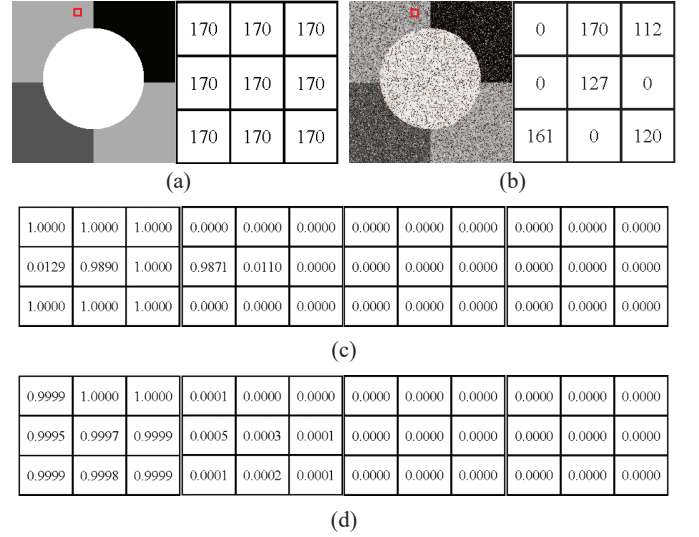


Fig. 4. Comparison of partition matrices generated by the FCM algorithm and KL divergence-based FCM algorithm. (a) Original image. (b) Observed image. (c) Membership partition using the FCM algorithm. (d) Membership partition using the KL divergence-based FCM algorithm.

D. Reconstruction of Segmented Feature Set

To further improve the KL divergence-based FCM algorithm, we conduct the reconstruction for the segmented feature set. Here we denote the obtained partition matrix and prototypes as $\mathbf{U}^* = [u_{ij}^*]_{c \times K}$ and $\mathbf{V}^* = \{\mathbf{v}_i^*\}_{i=1,2,\dots,c}$. Based on them, we obtain the segmented feature set $\bar{\mathbf{X}}$ that contains c prototypes. The filtered partition matrix corresponding to \mathbf{U}^* is denoted as $\bar{\mathbf{U}}^* = [\bar{u}_{ij}^*]_{c \times K}$. By their assistance, we reconstruct the segmented feature set by minimizing the inverse process of (4), i.e.,

$$J(\tilde{\mathbf{X}}) = \sum_{i=1}^c \sum_{j=1}^K u_{ij}^* (\|\tilde{\mathbf{x}}_j - \mathbf{v}_i^*\|^2 + \alpha \|\bar{\tilde{\mathbf{x}}}_j - \mathbf{v}_i^*\|^2) + \beta \sum_{i=1}^c \sum_{j=1}^K u_{ij}^* \log \frac{u_{ij}^*}{\bar{u}_{ij}^*}, \quad (8)$$

where $\tilde{\mathbf{X}} = \{\tilde{\mathbf{x}}_j\}_{j=1,2,\dots,K}$ is the reconstructed feature set and $\sum_{i=1}^c u_{ij}^* = 1$ always holds. Obviously, there exists an unknown $\tilde{\mathbf{X}}$ in (8). Thus we can acquire reconstructed feature set $\tilde{\mathbf{X}}$ by solving

$$\frac{\partial J}{\partial \tilde{\mathbf{x}}_j} = 0.$$

The optimal $\tilde{\mathbf{x}}_j$ is presented as

$$\tilde{\mathbf{x}}_j = \sum_{i=1}^c u_{ij}^* \mathbf{v}_i^*. \quad (9)$$

In the reconstruction process, some differences between $\tilde{\mathbf{X}}$ and $\bar{\mathbf{X}}$ are encountered, which are produced by abnormal features in $\tilde{\mathbf{X}}$ that do not belong to $\bar{\mathbf{X}}$. To modify these features, for $j = 1, 2, \dots, K$, we substitute $\tilde{\mathbf{x}}_j$ by $\hat{\mathbf{x}}_j$ defined as

$$\hat{\mathbf{x}}_j = \mathbf{v}_i^*, \text{ for } i \in \{1, 2, \dots, c\}, \quad (10)$$

subject to

$$\|\tilde{\mathbf{x}}_j - \mathbf{v}_i^*\| = \min\{\|\mathbf{x}_j - \mathbf{v}_1^*\|, \dots, \|\mathbf{x}_j - \mathbf{v}_c^*\|\}.$$

All elements $\{\hat{x}_j\}_{j=1,2,\dots,K}$ make up the modified feature set $\widehat{\mathbf{X}}$.

To intuitively show the effect of the reconstruction process, we take a case in which tight wavelet frames are absent. We choose the noisy image as shown in Fig. 4(b). We set $c = 4$, $\alpha = 1.5$, and $\beta = 15000$. The obtained results are displayed in Fig. 5.

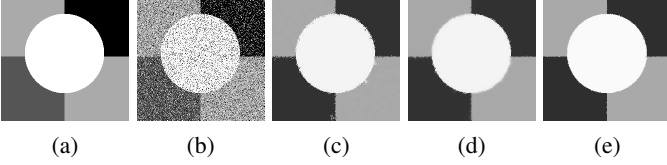


Fig. 5. Investigation of the reconstruction process. (a) Original image; (b) Observed image; (c) Segmented image via KL divergence; (d) Reconstructed image; (e) Modified image.

Fig. 5 indicates the segmentation result obtained by using the KL divergence is unsatisfactory to certain extent. In the reconstruction process, some blurred edges are produced. Thus, the reconstructed image contains more than four gray levels. Whereas, these blurred edges are eliminated in the modification process.

E. Reconstruction of Segmented Image

Once the modified feature set are obtained, we reconstruct the segmented image \tilde{f} using the wavelet frame reconstruction operator \mathcal{W}^T , i.e.,

$$\tilde{f} = \mathcal{W}^T(\widehat{\mathbf{X}}). \quad (11)$$

Hence, the proposed algorithm is realized as **Algorithm 1**.

Algorithm 1 KL divergence-based FCM algorithm incorporating the MR and wavelet frames (KLDFCM)

Input: Image f , number of clusters c , and threshold ε .

Output: Segmented image \tilde{f} .

- 1: Calculate the filtered image \bar{f} via (2)
 - 2: Calculate the feature sets \mathbf{X} and $\widehat{\mathbf{X}}$ via (3)
 - 3: Initialize randomly the filtered partition matrix $\bar{\mathbf{U}}^{(0)}$ and prototypes $\mathbf{v}_i^{(0)}$
 - 4: $t \leftarrow 1$
 - 5: **repeat**
 - 6: Calculate the partition matrix $\mathbf{U}^{(t)}$ using the filtered partition matrix $\bar{\mathbf{U}}^{(t-1)}$ and prototypes $\mathbf{v}_i^{(t-1)}$ via (6)
 - 7: Update the filtered partition matrix $\bar{\mathbf{U}}^{(t)}$ via (5)
 - 8: Update the prototypes $\mathbf{v}_i^{(t)}$ by using the partition matrix $\mathbf{U}^{(t)}$ via (7)
 - 9: $t \leftarrow t + 1$
 - 10: **until** $\|\mathbf{U}^{(t)} - \mathbf{U}^{(t-1)}\| < \varepsilon$
 - 11: **return** prototypes \mathbf{v}_i , partition matrix \mathbf{U} , and filtered partition matrix $\bar{\mathbf{U}}$
 - 12: Calculate the reconstructed feature set $\widetilde{\mathbf{X}}$ via (9)
 - 13: Calculate the modified feature set $\widehat{\mathbf{X}}$ via (10)
 - 14: Calculate the segmented image \tilde{f} via (11)
-

IV. EXPERIMENTAL STUDIES

In this section, we complete a collection of numerical experiments to verify the effectiveness and efficiency of the proposed algorithm. We provide KLDFCM's segmentation results reported for synthetic, medical, and color images. Moreover, we also make some comparisons between KLDFCM and eight existing algorithms in the literature, including 'FCM_S1' [7], 'FCM_S2' [7], 'FGFCM' [8], 'FLICM' [9], 'KWFLICM' [11], 'FRFCM' [18], 'WFCM' [13], and 'DSFCM_N' [19].

Besides visual comparisons, we also display segmentation comparisons in a quantitative fashion. Here, we employ two performance indicators, i.e., segmentation accuracy (SA) [33] and entropy-based information (EI) [34]. The SA is often used to assess the performance of segmenting images with known ground truth. The larger the SA value is, the better the segmentation effect becomes. The essence of index EI is to minimize the uniformity across all clusters by maximizing the uniformity of pixels within each segmented cluster. Hence, the better segmentation effect is associated with a smaller EI value.

A. Parameter Setting

Before conducting all numerical experiments, we introduce parameter settings in all algorithms. Since all comparative algorithms take spatial information of observed images into account, we fairly select a local window with size 3×3 . We set fuzzification coefficient $m = 2$ across eight comparative algorithms, and threshold $\varepsilon = 1 \times 10^{-6}$ across all algorithms. The number of clusters c is assumed to be known, and preset to the same for all algorithms. It is noted that KLDFCM is free of m .

Except for m , ε , and c , we next introduce how to set the remaining parameters in all comparative algorithms. α in FCM_S1 and FCM_S2 is experimentally set to 3.8, which is used to control the impact of the neighborhood term on FCM. In FGFCM, we set the spatial scale factor λ_s and the gray-level scale factor λ_g to 3 and 5, respectively. There exist no more parameters in FLICM and KWFLICM. For FRFCM, the observed image is selected as the mask image and the marker image is obtained by a square structuring element of size 3×3 . What's more, a median filter with window size 3×3 is applied to the fuzzy membership filtering. As to WFCM, μ controls the impact of the spatial information on FCM, which is determined experimentally with the values in range of $[0.55, 0.65]$. For DSFCM_N, p is set to 1 and the parameter vector λ is selected according to the standard deviation of each channel of image data.

In the following, we discuss how to set the remaining parameters of the KLDFCM. To apply the MR to filter image pixels, we select the same parameters as those in FRFCM. For the tight wavelet frame transform, we set its level to 1. A median filter with window size 3×3 is applied to the membership filtering. Beyond that, there only exist two parameter α and β in KLDFCM. Here, we report two examples to exhibit how to select α and β . We impose mixed Gaussian and impulse noise with $s = 30$ and $r = 20\%$ on three synthetic images with ground truth, refer to Fig. 8(a)–(c). By fixing

$\beta = 15000$ in advance, we first take a set of values of α to show the change of segmentation performance of the proposed algorithm. As shown in Fig. 6, with the increase of α , the SA value keeps increasing until it reaches the maximum. After that, the SA value slowly decreases. In order to provide a reference for parameter selection in the following experiments, we can determine α experimentally within the range $[0.5, 1.5]$.

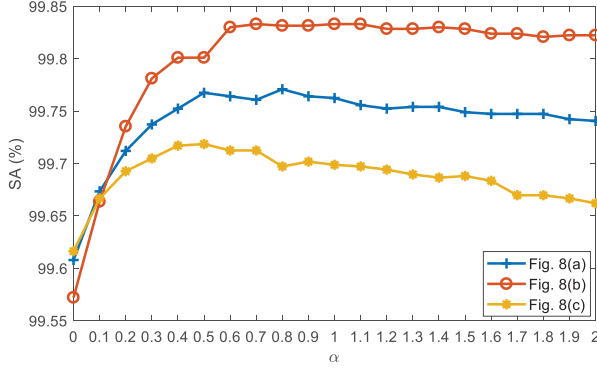


Fig. 6. Segmentation accuracy versus values of α .

For selection of β , by fixing $\alpha = 1$, we take a sequence of values of β to investigate their impacts on the segmentation effects of the proposed algorithm. β is increased from an initial value. Here, we set the initial value to 5,000 for all tested examples. As shown in Fig. 7, there exists a maximum of SA as β increases. To simplify parameter settings of the following experiments, we choose $\beta \in [10000, 45000]$ experimentally.

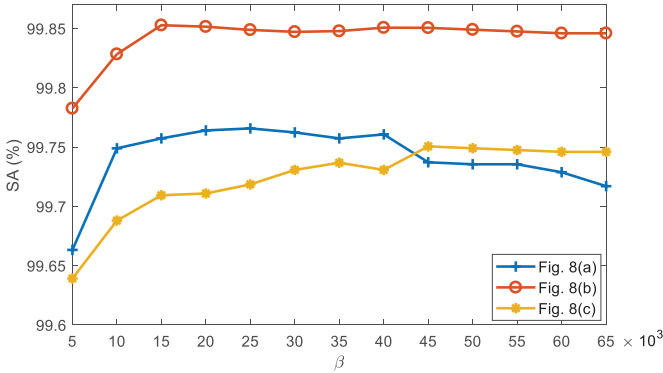


Fig. 7. Segmentation accuracy versus values of β .

B. Ablation Studies and Analysis

This work involves four key components, i.e., image filtering, feature extraction, KL divergence, and feature set reconstruction. In the following, we conduct ablation studies to exhibit the impact of each component on the proposed algorithm. The mixed Gaussian and impulse noise with $s = 30$ and $r = 20\%$ is imposed on the image shown in Fig. 8(b). The number of clusters is set to 4. We select $\alpha = 1$ and $\beta = 15000$. The level of tight wavelet frame transform is 1. The results are represented in TABLE I, which are obtained after several runs. The symbol \checkmark represents the corresponding component is considered to enable while symbol \times indicates that the corresponding component becomes absent.

TABLE I
INVESTIGATION OF EACH COMPONENT IN THE PROPOSED ALGORITHM

Image filtering	Feature extraction	KL divergence	Feature set reconstruction	SA (%)	Iterations
\times	\times	\times	\times	91.9734	27
\checkmark	\times	\times	\times	98.7976	46
\times	\checkmark	\times	\times	92.5247	23
\times	\times	\checkmark	\times	99.6536	112
\times	\times	\times	\checkmark	92.4194	27
\checkmark	\checkmark	\checkmark	\times	99.7528	129
\checkmark	\checkmark	\times	\checkmark	98.7976	46
\checkmark	\times	\checkmark	\checkmark	99.6811	119
\times	\checkmark	\checkmark	\checkmark	99.6536	112
\checkmark	\checkmark	\checkmark	\checkmark	99.8513	129

Obviously, we test 10 different combinations of the four key components. Here, we clarify that a small value of β is chosen, i.e., $\beta = 60$, in order to make (6) executable, which represents that the KL divergence is absent. When all components are absent, the SA result of FCM is only 91.9734%. By considering each component alone, we can find the SA values are increased by 6.8242%, 0.5513%, 7.6802%, and 0.4460%, respectively. Therefore, compared with feature extraction and feature set reconstruction, the image filtering has a relatively larger influence on the performance improvement of FCM. Except for the KL divergence, other three components are time-saving. In addition, the KL divergence has the greatest impact on the improvement of the segmentation performance of FCM. However, it also gives rise to high computation costs. Nevertheless, the computational efficiency of the proposed algorithm is still very high since spatial information is not computed in each iteration, which thanks to the use of the MR.

C. Results for Synthetic Images

We first conduct numerical experiments of segmenting six synthetic images, including three images with ground truth (refer to Fig. 8(a)–(c)) and three images without ground truth (refer to Fig. 8(d)–(f)). The numbers of clusters of six synthetic images are set to 4, 4, 4, 2, 2, and 2, respectively. To exhibit KLDFCM's robustness to multiple noise, we impose mixed Gaussian and impulse noise on all images. The level of Gaussian noise is 30. The density of impulse noise is 15%. In particular, we remove salt and pepper impulse noise since it is one of the most common types of impulse noise. The segmentation results are illustrated in Fig. 9 and TABLE II.

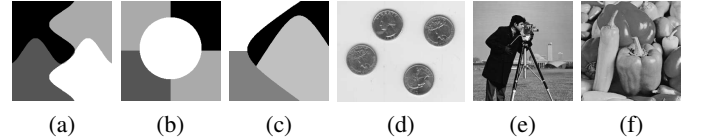


Fig. 8. Six synthetic images.

As shown in Fig. 9, we clearly observe that FCM_S1, FCM_S2, FGFCM and FLICM are not capable to suppress mixed noise. Compared with them, KWFLICM and WFCM can remove a large proportion of mixed noise. Even though FRFCM and DSFCM_N exhibit the superior performance for mixed noise removal, they change image edges to some

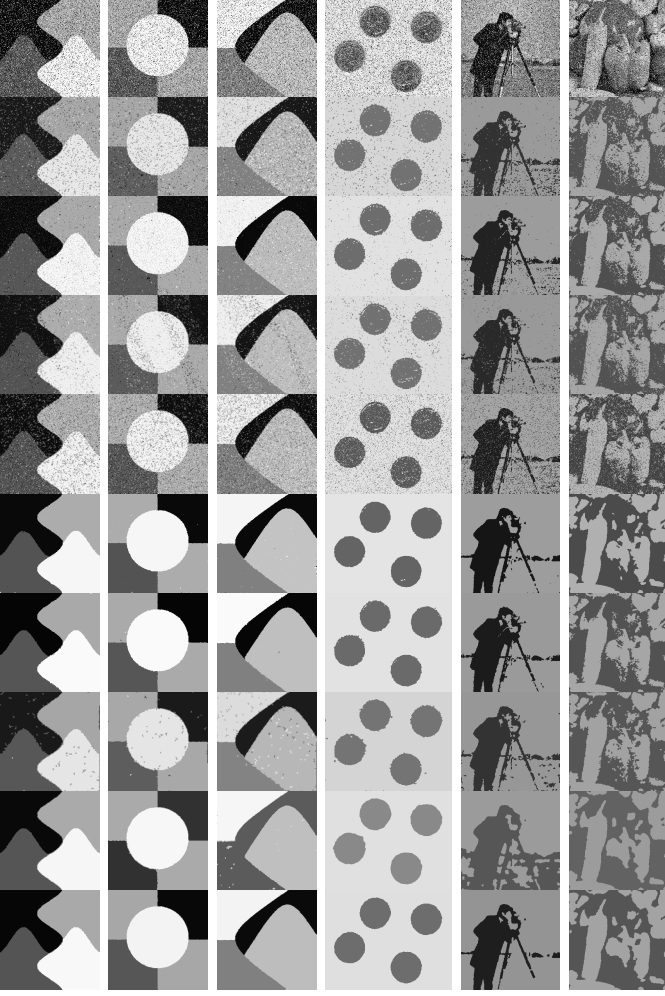


Fig. 9. Segmentation results on synthetic images corrupted by mixed Gaussian and impulse noise. The parameters: $\alpha_1 = 0.8$, $\beta_1 = 25000$; $\alpha_2 = 0.7$, $\beta_2 = 15000$; $\alpha_3 = 0.5$, $\beta_3 = 45000$; $\alpha_4 = 0.5$, $\beta_4 = 15000$; $\alpha_5 = 1.5$; $\beta_5 = 20000$; and $\alpha_6 = 1$, $\beta_6 = 15000$. From top to bottom: noisy images and results of FCM_S1, FCM_S2, FGFCM, FLICM, KWFLICM, FRFCM, WFCM, DSFCM_N, and KLDFCM.

extents. Superior to these comparative algorithms, KLDFCM can efficiently remove mixed noise and preserve clear image details.

TABLE II reports the quantitative results (SA and EI) for segmenting synthetic images. In presence of mixed noise of a high intensity, the superiority of KLDFCM is apparent. For synthetic images with ground truth, the SA value of KLDFCM is up to 99.9630% on Fig. 8(a). As to synthetic images without ground truth, the EI value of KLDFCM is down to 1.4814 on Fig. 8(d). Compared with KLDFCM, other comparative algorithms reveal the worse EI results while copying with mixed noise of a high intensity.

D. Results for Medical Images

In this subsection, we segment magnetic resonance images (MRIs) coming from a simulated brain database (BrainWeb): <http://www.bic.mni.mcgill.ca/brainweb/>. MRIs are generated by T1 modality with slice thickness of 1mm resolution, 9% noise and 20% intensity non-uniformity. As shown in Fig. 10,

TABLE II
SEGMENTATION RESULTS ON SIX SYNTHETIC IMAGES

Method	Fig. 8(a)	Fig. 8(b)	Fig. 8(c)	Fig. 8(d)	Fig. 8(e)	Fig. 8(f)
FCM_S1	97.1144	96.5805	98.6084	1.5457	2.1894	2.3797
FCM_S2	98.6294	98.3917	99.6048	1.5071	2.1642	2.3495
FGFCM	98.2280	96.4813	98.2849	1.5328	2.1890	2.3803
FLICM	93.1907	92.7856	75.9262	1.5940	2.2378	2.4226
KWFLICM	99.8992	99.8932	99.8901	1.4842	2.1445	2.3042
FRFCM	99.9009	99.8505	99.8642	1.4854	2.1447	2.3184
WFCM	99.4793	99.0738	99.4675	1.4908	2.1624	2.3330
DSFCM_N	99.6288	99.5743	80.7983	1.4834	2.2090	2.3116
KLDFCM	99.9630	99.9054	99.8967	1.4814	2.1396	2.2974

we select five slices in the axial plane with the sequence of 70, 80, 90, 100, and 110.

Fig. 10 reports visual comparisons for segmenting five MRIs. The numbers of clusters are set to 4. The corresponding quantitative comparisons are summarized in TABLE III. As shown in Fig. 10, KLDFCM maintains clear contours in images while other FCM-related algorithms generate several shape changes such as merging and splitting. TABLE III shows that KLDFCM universally acquires the larger SA values than other eight algorithms. In particular, the SA value of KLDFCM comes up to 99.1953% for the fourth slice in Fig. 10. Therefore, we conclude that KLDFCM is superior to other existing algorithms when segmenting MRIs.

TABLE III
SA RESULTS (%) ON FIVE MRIS

Method	Fig. 10 row 1	Fig. 10 row 2	Fig. 10 row 3	Fig. 10 row 4	Fig. 10 row 5
FCM_S1	98.1261	98.3553	98.699	98.8823	95.4732
FCM_S2	98.3502	98.4087	98.7015	98.8899	98.6913
FGFCM	97.6246	97.4794	97.9759	98.2101	95.6438
FLICM	98.3044	98.3553	98.7474	98.8874	98.7219
KWFLICM	97.3343	97.9174	98.0421	98.5411	98.536
FRFCM	97.9123	97.9708	98.5360	98.6506	98.5742
WFCM	97.4973	97.6042	98.2025	98.3986	98.5292
DSFCM_N	92.5784	92.0055	98.3731	98.6022	95.6921
KLDFCM	99.0302	98.6934	99.2031	99.1953	99.0269

E. Results for Color Images

Besides gray images, we also consider a series of Red-Green-Blue (RGB) color images. Generally speaking, most of FCM-related algorithms are not applicable to color image segmentation since spatial information of color images is hard to acquire. Whereas, KLDFCM overcomes this shortcoming. In addition, we easily extend KLDFCM to color image segmentation. The multivariate MGR can be applied to RGB color images [35]. As to the tight wavelet frame transform, we apply it to feature extraction in each channel of a RGB color image. Hence, the dimensionality of the obtained feature set is triple that of a gray image. The remaining operations of color image segmentation are similar to those of gray image segmentation. To further demonstrate the performance for color image segmentation, we segment two sets of color images.

We first segment six color images that are borrowed from the Berkeley Segmentation Dataset (BSDS300): <https://www2.eecs.berkeley.edu/Research/Projects/CS/vision/bsds/>

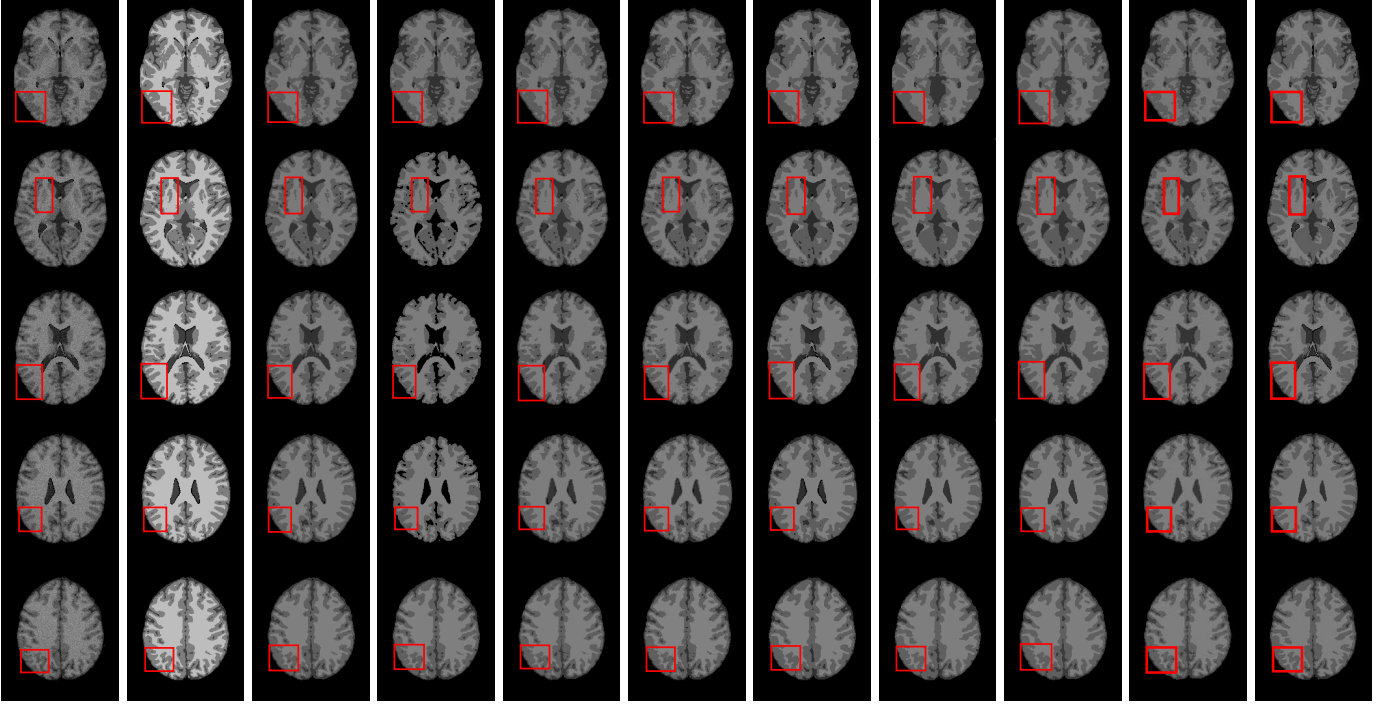


Fig. 10. Segmentation results on five MRIs. The parameters: $\alpha = 0.8$ and $\beta = 10000$. From left to right: noisy images, ground truth, and results of FCM_S1, FCM_S2, FGFCM, FLICM, KWFLICM, FRFCM, WFCM, DSFCM_N, and KLDFCM.

BSDS300/html/dataset/images.html. We set the numbers of clusters to 2, 2, 2, 3, 2, 2, respectively. The relevant segmentation results are shown in Fig. 11 and TABLE IV. Obviously, except for FRFCM and WFCM, other comparative algorithms perform poorly. Although FRFCM and WFCM mostly retain image contours, they result in several shape changes. Superior to them, the segmentation results of KLDFCM are closer to true segmentation results. TABLE IV illustrates the EI results of segmenting six color images. The EI values of KLDFCM are everywhere smaller than those of other comparative algorithms, which indicates that KLDFCM acquires better uniformity in segmented images. Therefore, we conclude that KLDFCM can achieve excellent performance for segmenting color images.

TABLE IV
EI RESULTS ON SIX COLOR IMAGES IN BSDS300

Method	Fig. 11 row 1	Fig. 11 row 2	Fig. 11 row 3	Fig. 11 row 4	Fig. 11 row 5	Fig. 11 row 6
FCM_S1	2.2468	1.6699	1.9991	2.1728	2.1993	2.0762
FCM_S2	2.2813	1.6650	1.9953	2.1696	2.1996	2.0771
FGFCM	2.2689	1.7014	2.0231	2.1906	2.2306	2.0834
FLICM	2.2336	1.6556	2.1135	2.2658	2.2014	2.0725
KWFLICM	2.2598	1.6176	2.1404	2.3190	2.2160	2.0830
FRFCM	2.1503	1.5173	2.0376	2.2180	2.1427	1.9821
WFCM	2.1483	1.5176	2.0404	2.2190	2.1160	1.9830
DSFCM_N	2.3065	1.6895	2.1353	2.2466	2.2355	2.1828
KLDFCM	2.1336	1.5074	1.9840	2.1409	2.1155	1.9786

Besides simulated color images mentioned above, we also consider segmenting real-world images coming from the NASA Earth Observation database: <http://neo.sci.gsfc.nasa.gov/>. In general, there exists unknown noise in sampled images due to bit errors appearing in satellite measurements.

We choose two real-world images representing two specific scenes, i.e., sea ice and snow extent and chlorophyll concentration. Due to the lack of reference (original) images, index EI cannot directly used. Hence, we randomly shoot each scene for 50 times within the time span 2000–2019, which generates the mean image. It can be taken as the reference image. The calculated EI results are given in TABLE V. The corresponding visual comparisons are presented in Fig. 12.

TABLE V
EI RESULTS ON TWO REAL-WORLD IMAGES IN NASA

Method	Fig. 12 row 1	Fig. 12 row 2
FCM_S1	0.8713	1.4995
FCM_S2	0.8516	1.5016
FGFCM	0.8840	1.5107
FLICM	0.8592	1.4885
KWFLICM	0.8312	1.4994
FRFCM	0.8146	1.3700
WFCM	0.8172	1.3952
DSFCM_N	0.8725	1.5058
KLDFCM	0.7860	1.3111

The first row of Fig. 12 reports the segmentation results on a real-world image showing sea ice and snow extent. The colors represent where the land and ocean are covered by snow and ice per week (here is February 7–14, 2015). We set $c = 4$. The second row of Fig. 12 illustrates the results for segmenting a real-world image showing chlorophyll concentration. The colors represent where and how much phytoplankton are growing over a span of days. The black areas show where the satellite could not measure phytoplankton. We set $c = 2$. As shown in Fig. 12, there exists the remaining noise in the segmented results of FCM_S1, FCM_S2, FGFCM, FLICM,

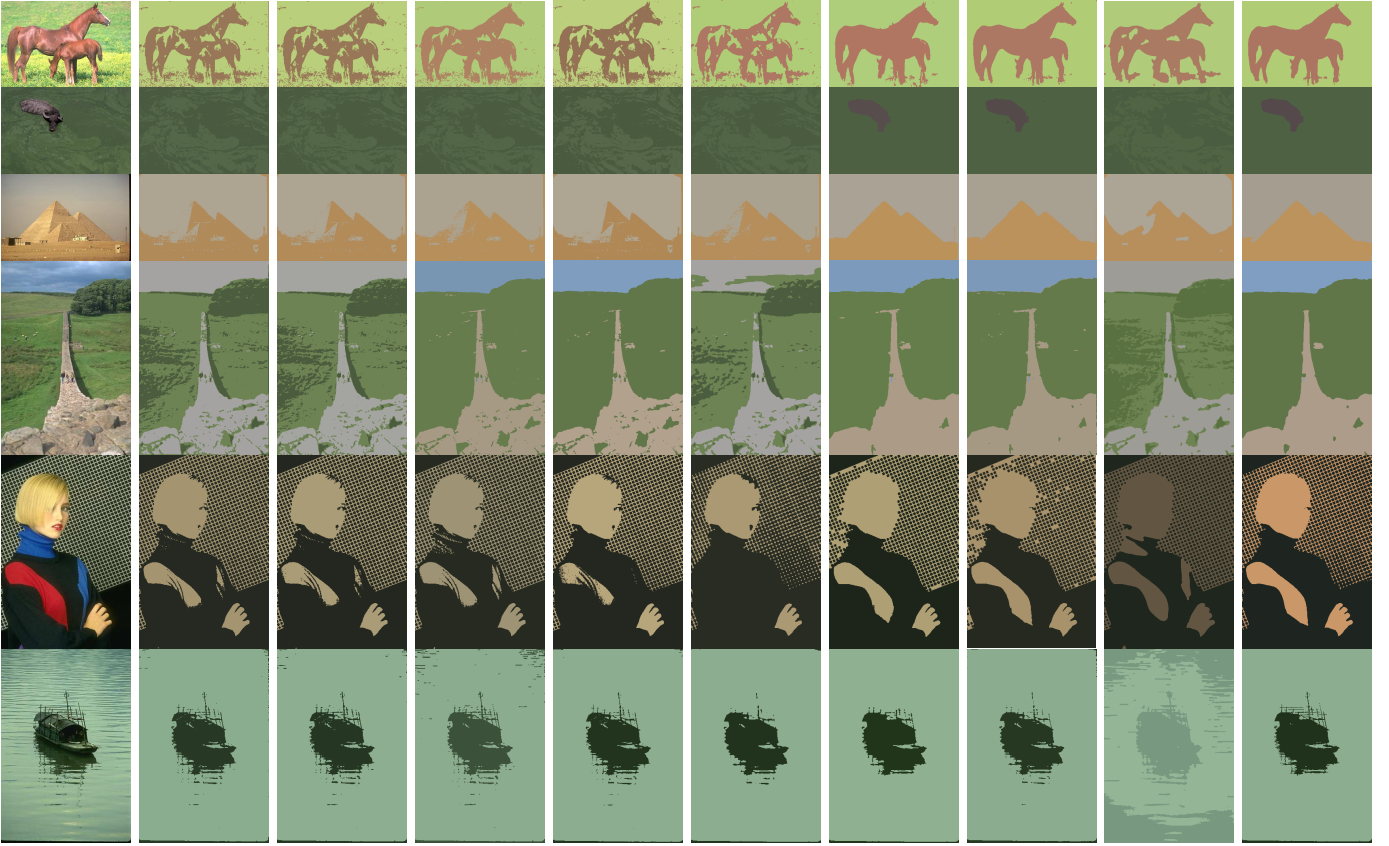


Fig. 11. Segmentation results on six color images in BSDS300. The parameters: $\alpha_1 = 0.8$, $\beta_1 = 10000$; $\alpha_2 = 0.5$, $\beta_2 = 15000$; $\alpha_3 = 0.7$, $\beta_3 = 25000$; $\alpha_4 = 0.5$, $\beta_4 = 10000$; $\alpha_5 = 0.8$; $\beta_5 = 20000$; and $\alpha_6 = 0.5$, $\beta_6 = 10000$. From left to right: original images and results of FCM_S1, FCM_S2, FGFCM, FLICM, KWFLICM, FRFCM, WFCM, DSFCM_N, and KLDFCM.

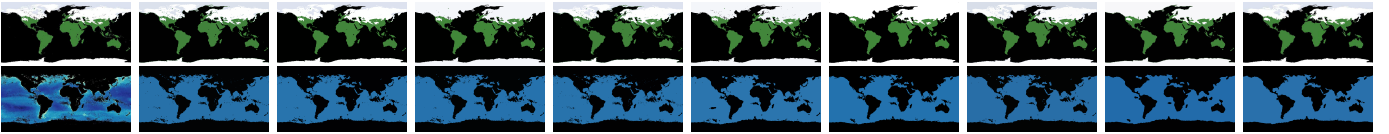


Fig. 12. Segmentation results on two real-world images ($\alpha_1 = 1.5$, $\beta_1 = 10000$ and $\alpha_2 = 1$, $\beta_2 = 15000$). From left to right: noisy images and results of FCM_S1, FCM_S2, FGFCM, FLICM, KWFLICM, FRFCM, WFCM, DSFCM_N, and KLDFCM.

KWFLICM, and WFCM. Although FRFCM and DSFCM_N can sufficiently remove unknown noise, they give rise to over-smoothing to some extent. What's worse, there exist several topological changes including merging and splitting in the segmentation results of the two algorithms. Compared with other comparative algorithms, KLDFCM not only fully removes unknown noise, but also remains clear edges in images. In the light of the visual results shown in Fig. 12 and quantitative comparisons in TABLE V, it is concluded that KLDFCM overcomes the drawback of other FCM-related algorithms.

F. Computing Overhead

To illustrate the efficiency of above FCM-related algorithms, we compare the computing overhead of KLDFCM with those of other algorithms. For fair comparison, we clarify that all experiments are completed in MATLAB on a laptop with Intel(R) Xeon(R) W-2133 CPU of (3.60 GHz) and 32.0 GB RAM.

More specifically, we here demonstrate the average computing overheads of copying with different types of images, including synthetic images with ground truth, synthetic images without ground truth, medical images, color images and real-world images. The relevant results are shown in Fig. 13.

As shown in Fig. 13, when segmenting gray images, FCM_S1, FCM_S2 and KWFLICM are time-consuming. In comparison, the remaining algorithms present sound computational efficiency. Especially, FRFCM is the most time-saving due to the usage of gray level histograms. Except for FRFCM, the efficiency of KLDFCM is higher than those of all other algorithms. As to color image segmentation, it is apparent that KWFLICM is the most time-consuming. Compared with other algorithms, FRFCM and KLDFCM exhibit lower computational complexities. It is worth noting that the efficiency of KLDFCM is slightly lower than that of FRFCM. However, the drawback can be tolerated due to its better segmentation effects. Therefore, KLDFCM is more practical since it has acceptable computing overhead and better

segmentation performance simultaneously.

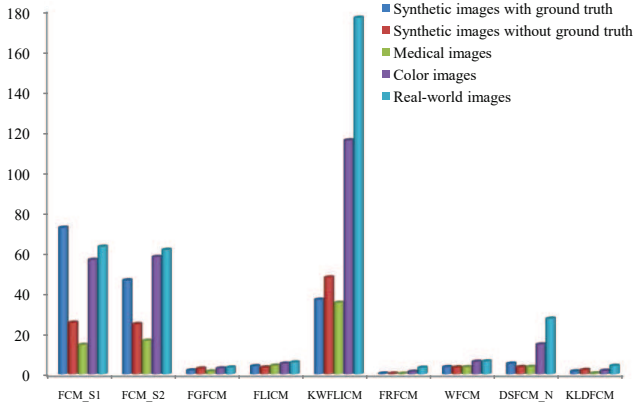


Fig. 13. Average computing overheads (in seconds) on different types of images.

V. CONCLUSIONS

To retain a meaningful trade-off between the segmentation performance and the speed of clustering, we report a KL divergence-based FCM algorithm by incorporating a tight wavelet frame transform and the MR. At the inception, an observed image is filtered by using the MR. A tight wavelet frame system is employed to decompose the observed and filtered images so as to form their feature sets. Taking these feature sets as data of clustering, we present the modified FCM algorithm that incorporates a KL divergence term in the partition matrix into its objective function. Whereafter, we design a reconstruction process on the segmented feature set. As a result, the segmentation accuracy of KL divergence-based FCM is further improved. Moreover, we provide supporting experiments to show the effectiveness of the proposed algorithm. Finally, we conclude this work as follows:

- 1) As a pre-processing step, the MR introduce spatial information into FCM, which means the iterative calculation of a conventional local neighbor term is avoided. Thus the proposed algorithm is not time-consuming. In addition, the MR exhibits the noise-immunity and retention capacity of image details, which improves the robustness of FCM.
- 2) A tight wavelet frame transform is used to form feature sets of images, which thereby eliminates the defect of using image pixels. Hence, the underlying features in images can be analyzed as much as possible. Moreover, tight wavelet frames can be viewed as a kernel function, thus forming a kernel-based FCM algorithm.
- 3) A KL divergence term in the partition matrix is introduced into the objective function of FCM, which gives rise to the optimal partition matrix. Thus, it improves the segmentation performance. In addition, we design the reconstruction of the segmented feature set in order to further enhance the segmentation effects. Finally, the usage of KL divergence makes the fuzzification coefficient nor present in the FCM algorithm. Hence, the parameter setting of FCM is simplified.

- 4) The segmentation results of the proposed algorithm indicate that it has good performance for image segmentation. Moreover, the proposed algorithm is superior to other existing algorithms.
- 5) The proposed algorithm exhibits high computational efficiency. Even though it is slightly slower than few algorithms, its good performance can overcome this drawback.

Experimental results illustrate that the proposed algorithm is effective and practical. However, there are some open issues worth pursuing. For instance, the application areas of the proposed algorithm can be further expanded to image segmentation in non-flat domains, such as remote sensing [36], computer networks, ecological systems [37], and transportation networks [38]. The values of the parameters might also be automatically chosen. Moreover, the automatic setting of numbers of clusters can be further discussed.

APPENDIX

Consider the minimization of the objective function

$$J(U, V) = \sum_{i=1}^c \sum_{j=1}^K u_{ij} (\|x_j - v_i\|^2 + \alpha \|\bar{x}_j - v_i\|^2) + \beta \sum_{i=1}^c \sum_{j=1}^K u_{ij} \log \frac{u_{ij}}{\bar{u}_{ij}},$$

subject to

$$\sum_{i=1}^c u_{ij} = 1 \text{ for } j \in \{1, 2, \dots, K\}.$$

We apply the Lagrangian multiplier method to solve the minimization problem. The Lagrangian function is formulated as

$$\mathcal{L}_\Lambda(U, V) = \sum_{i=1}^c \sum_{j=1}^K u_{ij} d_{ij} + \beta \sum_{i=1}^c \sum_{j=1}^K u_{ij} \log \frac{u_{ij}}{\bar{u}_{ij}} + \sum_{j=1}^K \lambda_j \left(\sum_{i=1}^c u_{ij} - 1 \right), \quad (12)$$

where $\Lambda = \{\lambda_j : j = 1, 2, \dots, K\}$ stands for a set of the Lagrangian multipliers, and $d_{ij} = \|x_j - v_i\|^2 + \alpha \|\bar{x}_j - v_i\|^2$.

First, by fixing V , we minimize (12) in terms of the partition matrix U . Thus, we have

$$\frac{\partial \mathcal{L}_\Lambda}{\partial u_{ij}} = d_{ij} + \beta \left(\log \frac{u_{ij}}{\bar{u}_{ij}} + 1 \right) + \lambda_j = 0.$$

We obtain

$$u_{ij} = \bar{u}_{ij} e^{-d_{ij}/\beta} \cdot \frac{1}{e^{\lambda_j/\beta+1}}. \quad (13)$$

Based on the constraint $\sum_{q=1}^c u_{qj} = 1$, we have

$$\begin{aligned} 1 &= \sum_{q=1}^c u_{qj} = \sum_{q=1}^c \left(\bar{u}_{qj} e^{-d_{qj}/\beta} \cdot \frac{1}{e^{\lambda_j/\beta+1}} \right) \\ &= \frac{1}{e^{\lambda_j/\beta+1}} \sum_{q=1}^c \bar{u}_{qj} e^{-d_{qj}/\beta}. \end{aligned}$$

Thus, we get

$$\frac{1}{e^{\lambda_j/\beta+1}} = 1 / \sum_{q=1}^c \bar{u}_{qj} e^{-d_{qj}/\beta}. \quad (14)$$

Substituting (14) into (13), we acquire

$$u_{ij} = \frac{\bar{u}_{ij} e^{-d_{ij}/\beta}}{\sum_{q=1}^c \bar{u}_{qj} e^{-d_{qj}/\beta}}.$$

Next, by fixing U , we minimize (12) in terms of V . Thus, we have

$$\frac{\partial \mathcal{L}_\lambda}{\partial v_i} = \sum_{j=1}^K (-2) \cdot u_{ij} \cdot ((x_j + \alpha \bar{x}_j) - (v_i + \alpha v_i)) = 0.$$

With that,

$$\sum_{j=1}^K u_{ij}(x_j + \alpha \bar{x}_j) = \sum_{j=1}^K u_{ij}(v_i + \alpha v_i).$$

The optimal v_i is described as

$$v_i = \frac{\sum_{j=1}^K u_{ij}(x_j + \alpha \bar{x}_j)}{(1 + \alpha) \sum_{j=1}^K u_{ij}}.$$

REFERENCES

- [1] J. C. Dunn, "A fuzzy relative of the ISODATA process and its use in detecting compact well-separated clusters," *J. Cybernet.*, vol. 3, no. 3, pp. 32–57, 1973.
- [2] J. C. Bezdek, *Pattern Recognition with Fuzzy Objective Function Algorithms*. New York: Plenum Press, 1981.
- [3] L. Szilagyi, Z. Benyo, S. Szilagyi, and H. Adam, "MR brain image segmentation using an enhanced fuzzy C-means algorithm," in *Proc. 25th Annu. Int. Conf. IEEE EMBS*, Sep. 2003, pp. 724–726.
- [4] X. Zhu, W. Pedrycz, and Z. Li, "Granular encoders and decoders: a study in processing information granules," *IEEE Trans. Fuzzy Syst.*, vol. 25, no. 5, pp. 1115–1126, Oct. 2017.
- [5] T. Celik and H. K. Lee, "Comments on 'A robust fuzzy local information c-means clustering algorithm'," *IEEE Trans. Image Process.*, vol. 22, no. 3, pp. 1258–1261, Mar. 2013.
- [6] M. Ahmed, S. Yamany, N. Mohamed, A. Farag, and T. Moriarty, "A modified fuzzy C-means algorithm for bias field estimation and segmentation of MRI data," *IEEE Trans. Med. Imag.*, vol. 21, no. 3, pp. 193–199, Aug. 2002.
- [7] S. Chen and D. Zhang, "Robust image segmentation using FCM with spatial constraints based on new kernel-induced distance measure," *IEEE Trans. Syst. Man Cybern. Part B Cybern.*, vol. 34, no. 4, pp. 1907–1916, Aug. 2004.
- [8] W. Cai, S. Chen, and D. Zhang, "Fast and robust fuzzy c-means clustering algorithms incorporating local information for image segmentation," *Pattern Recognit.*, vol. 40, no. 3, pp. 825–838, Mar. 2007.
- [9] S. Krinidis and V. Chatzis, "A robust fuzzy local information C-means clustering algorithm," *IEEE Trans. Image Process.*, vol. 19, no. 5, pp. 1328–1337, Jan. 2010.
- [10] X. Bai, Y. Zhang, H. Liu, and Z. Chen, "Similarity measure-based possibilistic FCM with label information for brain MRI segmentation," *IEEE Trans. Cybern.*, vol. 49, no. 7, pp. 2618–2630, Jul. 2019.
- [11] M. Gong, Y. Liang, J. Shi, W. Ma, and J. Ma, "Fuzzy C-means clustering with local information and kernel metric for image segmentation," *IEEE Trans. Image Process.*, vol. 22, no. 2, pp. 573–584, Feb. 2013.
- [12] Z. Zhao, L. Cheng, and G. Cheng, "Neighbourhood weighted fuzzy c-means clustering algorithm for image segmentation," *IET Image Process.*, vol. 8, no. 3, pp. 150–161, Mar. 2014.
- [13] C. Wang, W. Pedrycz, J. Yang, M. Zhou, and Z. Li, "Wavelet frame-based fuzzy C-means clustering for segmenting images on graphs," *IEEE Trans. Cybern.*, to be published, doi: 10.1109/TCYB.2019.2921779.
- [14] K. P. Lin, "A novel evolutionary kernel intuitionistic fuzzy C-means clustering algorithm," *IEEE Trans. Fuzzy Syst.*, vol. 22, no. 5, pp. 1074–1087, Aug. 2014.
- [15] X. Zhu, W. Pedrycz, and Z. W. Li, "Fuzzy clustering with nonlinearly transformed data," *Appl. Soft Comput.*, vol. 61, pp. 364–376, Dec. 2017.
- [16] R. R. Gharieb, G. Gendy, A. Abdelfattah, and H. Selim, "Adaptive local data and membership based KL divergence incorporating C-means algorithm for fuzzy image segmentation," *Appl. Soft Comput.*, vol. 59, pp. 143–152, Oct. 2017.
- [17] J. Gu, L. Jiao, S. Yang, and F. Liu, "Fuzzy double c-means clustering based on sparse self-representation," *IEEE Trans. Fuzzy Syst.*, vol. 26, no. 2, pp. 612–626, Apr. 2018.
- [18] T. Lei, X. Jia, Y. Zhang, L. He, H. Meng, and K. N. Asoke, "Significantly fast and robust fuzzy c-means clustering algorithm based on morphological reconstruction and membership filtering," *IEEE Trans. Fuzzy Syst.*, vol. 26, no. 5, pp. 3027–3041, Oct. 2018.
- [19] Y. Zhang, X. Bai, R. Fan, and Z. Wang, "Deviation-sparse fuzzy c-means with neighbor information constraint," *IEEE Trans. Fuzzy Syst.*, vol. 27, no. 1, pp. 185–199, Jan. 2019.
- [20] J. F. Cai, B. Dong, S. Osher, and Z. Shen, "Image restoration: total variation, wavelet frames, and beyond," *J. Amer. Math. Soc.*, vol. 25, no. 4, pp. 1033–1089, May 2012.
- [21] B. Dong and Z. Shen, "MRA-based wavelet frames and applications," in *The Mathematics of Image Processing* (IAS Lecture Notes Series). Salt Lake City, UT, USA: Park City Mathematics Institute, 2010.
- [22] L. Najman and M. Schmitt, "Geodesic saliency of watershed contours and hierarchical segmentation," *IEEE Trans. Pattern Anal. Mach. Intell.*, vol. 18, no. 12, pp. 1163–1173, Dec. 1996.
- [23] L. Vincent, "Morphological grayscale reconstruction in image analysis: applications and efficient algorithms," *IEEE Trans. Image Process.*, vol. 2, no. 2, pp. 176–201, Apr. 1993.
- [24] J. C. Bezdek, R. Ehrlich, and W. Full, "FCM: The fuzzy C-means clustering algorithm," *Comput. Geosci.*, vol. 10, no. 2-3, pp. 191–203, 1984.
- [25] B. Dong, "Sparse representation on graphs by tight wavelet frames and applications," *Appl. Comput. Harmon. Anal.*, vol. 42, no. 3, pp. 452–479, May 2017.
- [26] C. Wang, Z. Yan, W. Pedrycz, M. Zhou, and Z. Li, "A weighted fidelity and regularization-based method for mixed or unknown noise removal from images on graphs," *IEEE Trans. Image Process.*, to be published, doi: 10.1109/TIP.2020.2969076.
- [27] C. Wang and J. Yang, "Poisson noise removal of images on graphs using tight wavelet frames," *Visual Comput.*, vol. 34, no. 10, pp. 1357–1369, Oct. 2018.
- [28] B. Dong, Q. T. Jiang, C. Q. Liu, and Z. Shen, "Multiscale representation of surfaces by tight wavelet frames with applications to denoising," *Appl. Comput. Harmon. Anal.*, vol. 41, no. 2, pp. 561–589, Sep. 2016.
- [29] J. Yang and C. Wang, "A wavelet frame approach for removal of mixed Gaussian and impulse noise on surfaces," *Inverse Probl. Imaging*, vol. 11, no. 5, pp. 783–798, Oct. 2017.
- [30] A. Ron and Z. Shen, "Affine systems in $L_2(\mathbb{R}^d)$: The analysis of the analysis operator," *J. Funct. Anal.*, vol. 148, no. 2, pp. 408–447, Aug. 1997.
- [31] J. Chen, C. Su, W. Grimson, J. Liu, and D. Shiue, "Object segmentation of database images by dual multiscale morphological reconstructions and retrieval applications," *IEEE Trans. Image Process.*, vol. 21, no. 2, pp. 828–843, Feb. 2012.
- [32] J. Yang, G. Zhu, D. Tong, L. Lu, and Z. Shen, "B-spline tight frame based force matching method," *J. Comput. Phys.*, vol. 362, no. 1, pp. 208–219, Jun. 2018.
- [33] C. Li, R. Huang, Z. Ding, J. C. Gatenby, D. N. Metaxas, and J. C. Gore, "A level set method for image segmentation in the presence of intensity inhomogeneities with application to MRI," *IEEE Trans. Image Process.*, vol. 20, no. 7, pp. 2007–2016, Jul. 2011.
- [34] H. Zhang, J. Fritts, and S. Goldman, "An entropy-based objective evaluation method for image segmentation," in *Proc. SPIE, Storage Retrieval Methods Appl. Multimedia*, vol. 5307, Jan. 2004, pp. 38–49.
- [35] T. Lei, Y. Zhang, Y. Wang, S. Liu, and Z. Guo, "A conditionally invariant mathematical morphological framework for color images," *Inf. Sci.*, vol. 387, pp. 34–52, May 2017.
- [36] T. Xu, L. Jiao, and W. J. Emery, "SAR image content retrieval based on fuzzy similarity and relevance feedback," *IEEE J. Sel. Topics Appl. Earth Observ. Remote Sens.*, vol. 10, no. 5, pp. 1824–1842, May 2017.
- [37] C. Wang, J. Chen, Z. Li, E. Nasr, and A. M. El-Tamimi, "An indicator system for evaluating the development of land-sea coordination systems: A case study of Lianyungang port," *Ecol. Indic.*, vol. 98, pp. 112–120, Mar. 2019.
- [38] Y. Lv, Y. Chen, X. Zhang, Y. Duan, and N. Li, "Social media based transportation research: the state of the work and the networking," *IEEE/CAA J. Autom. Sinica*, vol. 4, no. 1, pp. 19–26, Jan. 2017.



Cong Wang received the B.S. degree in automation and the M.S. degree in mathematics from Hohai University, Nanjing, China, in 2014 and 2017, respectively. He is currently pursuing the Ph.D. degree in mechatronic engineering, Xidian University, Xi'an, China.

He was a Visiting Ph.D. Student with the Department of Electrical and Computer Engineering, University of Alberta, Edmonton, AB, Canada. He is currently a Research Assistant at the School of Computer Science and Engineering, Nanyang Technological University, Singapore. His current research interests include wavelet analysis and its applications, granular computing, and pattern recognition and image processing.



Witold Pedrycz (M'88-SM'90-F'99) received the MS.c., Ph.D., and D.Sci., degrees from the Silesian University of Technology, Gliwice, Poland.

He is a Professor and the Canada Research Chair in Computational Intelligence with the Department of Electrical and Computer Engineering, University of Alberta, Edmonton, AB, Canada. He is currently with the School of Electro-Mechanical Engineering, Xidian University, Xi'an 710071, China, and the Faculty of Engineering, King Abdulaziz University, Jeddah 21589, Saudi Arabia. He is also with the

Systems Research Institute of the Polish Academy of Sciences, Warsaw, Poland. He is a foreign member of the Polish academy of Sciences. He has authored 15 research monographs covering various aspects of computational intelligence, data mining, and software engineering. His current research interests include computational intelligence, fuzzy modeling, and granular computing, knowledge discovery and data mining, fuzzy control, pattern recognition, knowledge-based neural networks, relational computing, and software engineering. He has published numerous papers in the above areas.

Dr. Pedrycz was a recipient of the IEEE Canada Computer Engineering Medal, the Cajastur Prize for Soft Computing from the European Centre for Soft Computing, the Killam Prize, and the Fuzzy Pioneer Award from the IEEE Computational Intelligence Society. He is intensively involved in editorial activities. He is an Editor-in-Chief of Information Sciences, an Editor-in-Chief of WIREs Data Mining and Knowledge Discovery (Wiley) and the International Journal of Granular Computing (Springer). He currently serves as a member of a number of editorial boards of other international journals. He is a fellow of the Royal Society of Canada.



Zhiwu Li (M'06-SM'07-F'16) received the B.S. degree in mechanical engineering, the M.S. degree in automatic control, and the Ph.D. degree in manufacturing engineering from Xidian University, Xi'an, China, in 1989, 1992, and 1995, respectively.

He joined Xidian University in 1992. He is currently with the Institute of Systems Engineering, Macau University of Science and Technology, Macau, China. He was a Visiting Professor with the University of Toronto, Toronto, ON, Canada, the Technion-Israel Institute of Technology, Haifa,

Israel, the Martin-Luther University of Halle-Wittenburg, Halle, Germany, Conservatoire National des Arts et Métiers, Paris, France, and Meliksah Universitesi, Kayseri, Turkey. His current research interests include Petri net theory and application, supervisory control of discrete-event systems, workflow modeling and analysis, system reconfiguration, game theory, and data and process mining.

Dr. Li was a recipient of an Alexander von Humboldt Research Grant, Alexander von Humboldt Foundation, Germany. He is listed in Marquis Who's Who in the World, 27th Edition, 2010. He serves as a Frequent Reviewer of 90+ international journals, including Automatica and a number of the IEEE TRANSACTIONS as well as many international conferences. He is the Founding Chair of Xi'an Chapter of IEEE Systems, Man, and Cybernetics Society. He is a member of Discrete-Event Systems Technical Committee of the IEEE Systems, Man, and Cybernetics Society and IFAC Technical Committee on Discrete-Event and Hybrid Systems, from 2011 to 2014.



Mengchu Zhou (S'88-M'90-SM'93-F'03) received his B.S. degree in Control Engineering from Nanjing University of Science and Technology, Nanjing, China in 1983, M.S. degree in Automatic Control from Beijing Institute of Technology, Beijing, China in 1986, and Ph. D. degree in Computer and Systems Engineering from Rensselaer Polytechnic Institute, Troy, NY in 1990.

He joined New Jersey Institute of Technology (NJIT), Newark, NJ in 1990, and is now a Distinguished Professor of Electrical and Computer Engineering. He is also currently with the Institute of Systems Engineering, Macau University of Science and Technology, Macau 999078, China. His research interests are in Petri nets, intelligent automation, Internet of Things, big data, web services, and intelligent transportation.

He has over 800 publications including 12 books, 460+ journal papers (360+ in IEEE TRANSACTIONS), 12 patents and 29 book-chapters. He is the founding Editor of IEEE Press Book Series on Systems Science and Engineering and Editor-in-Chief of IEEE/CAA Journal of Automatica Sinica. He is a recipient of Humboldt Research Award for US Senior Scientists from Alexander von Humboldt Foundation, Franklin V. Taylor Memorial Award and the Norbert Wiener Award from IEEE Systems, Man and Cybernetics Society for which he serves as VP for Conferences and Meetings. He is a life member of Chinese Association for Science and Technology-USA and served as its President in 1999. He is a Fellow of International Federation of Automatic Control (IFAC), American Association for the Advancement of Science (AAAS) and Chinese Association of Automation (CAA).